

LETTER TO THE EDITOR

# Extremely iron-poor O-type stars in the Magellanic Bridge

E.C. Schösser<sup>1</sup>, V. Ramachandran<sup>1</sup>, A.A.C. Sander<sup>1</sup>, J.S. Gallagher<sup>2,3</sup>, M. Bernini-Peron<sup>1</sup>, G. González-Torà<sup>1</sup>, J. Josiek<sup>1</sup>, R.R. Lefever<sup>1</sup>, W.-R. Hamann<sup>4</sup>, and L.M. Oskinova<sup>4</sup>

<sup>1</sup> Zentrum für Astronomie der Universität Heidelberg, Astronomisches Rechen-Institut, Mönchhofstr. 12-14, 69120 Heidelberg, Germany

e-mail: elisa.schoesser@uni-heidelberg.de

<sup>2</sup> Department of Astronomy, University of Wisconsin, 475 N. Charter St., Madison, WI 53706, USA

<sup>3</sup> Department of Physics and Astronomy, Macalester College, 1600 Grand Ave, St. Paul, MN 55105 USA

<sup>4</sup> Institut für Physik und Astronomie, Universität Potsdam, Karl-Liebknecht-Str. 24/25, 14476 Potsdam, Germany

## ABSTRACT

**Context.** To study stars analogous to those in the early Universe with redshift  $z > 3$ , we need to probe environments with low metallicities. Until recently, massive O-type stars with metallicities lower than that of the Small Magellanic Cloud (SMC,  $Z < 20\%Z_{\odot}$ ) were only known in compact dwarf galaxies. Observations of stars in such distant galaxies ( $> 1$  Mpc) suffer from limited signal-to-noise ratios and spatial resolution. Recently, a few O-type stars were identified in the nearby Magellanic Bridge which offers a unique laboratory with low gas density and metal content.

**Aims.** We acquired high-resolution HST-COS FUV spectra of two O-type stars in the Magellanic Bridge. Using the UV forest of iron lines from these observations, we aim to precisely measure the inherent iron abundances and determine the metallicity of the stars.

**Methods.** Using detailed expanding non-LTE atmosphere models, we generate synthetic spectra for different iron abundances and for a range of microturbulent velocities. We use Bayesian posterior sampling to measure the iron abundance and compute uncertainties based on the possible range of microturbulent velocities.

**Results.** The O stars in the Magellanic Bridge have severely sub-SMC iron abundances, reaching as low as 10.8% and 3.6%  $\text{Fe}_{\odot}$ . The most Fe-deficient star also shows  $\alpha$ -enhancement. These stars are the nearest extremely metal-poor O stars discovered to date.

**Conclusions.** Our finding marks the first robust determination of O-star iron abundances in a metallicity regime comparable to dwarf galaxies like Sextans A and Leo P. The iron abundances of the stars do not correlate with their oxygen abundances. Our results highlight the problem of using oxygen-based metallicities. The proximity of the stars in the Bridge combined with their different abundance patterns underlines that the ISM of the Magellanic Bridge must be highly inhomogeneous and is not properly mixed.

**Key words.** stars: atmospheres – stars: abundances – stars: fundamental parameters – galaxies: Magellanic Clouds – stars: early-type – stars: massive

## 1. Introduction

Massive stars ( $M_{\text{init}} > 8 M_{\odot}$ ) play an important role for the chemical enrichment and ionization of the Universe. Following the Big Bang, the first Population III stars formed from pristine gas clouds which almost entirely consisted of hydrogen and helium (e.g. Bromm et al. 2002). Through nuclear fusion, these hot massive stars produced heavier elements (metals), primarily the  $\alpha$ -peak elements, which were dispersed into the interstellar medium (ISM) via intrinsic mass loss and their final core-collapse supernovae (see e.g. Woosley et al. 2002; Janka et al. 2007, for a review), seeding future generations of star formation.

Studying metal-poor massive stars, born in environments with minimal prior chemical enrichment, provides a unique window into the early stages of stellar evolution and nucleosynthesis. These stars are local analogs of the metal-poor stellar populations observed in high-redshift galaxies by the James Webb Space Telescope (JWST). The increasingly rich JWST spectroscopic observations of metal-deficient galaxies at high redshifts highlight the lack of a deeper quantitative understanding and problems in current models at low metallicity (see, e.g., Garg et al. 2024), e.g., when interpreting observed emission line ratios from ionized gas (Matthee et al. 2023; Laseter et al. 2024; Rowland et al. 2025). As discussed by Hopkins et al. (2023) the in-

terpretation of spatially integrated JWST spectra of most sources are expected to be affected by a variety of issues, such as dust absorption and ISM structure, as well as properties of the stars. Massive star models grounded by observational data are essential for the analysis of optical spectra of young, low-metallicity galaxies at high redshifts.

Empirical constraints from individual, observed metal-poor massive stars predominantly stem from spectroscopic studies of stars in the Small Magellanic Cloud (SMC) with a mean metallicity of  $Z \sim 20\% Z_{\odot}$  (e.g. Bouret et al. 2003; Ramachandran et al. 2019; Rickard et al. 2022) or within the recent “XShootU” collaboration (Vink et al. 2023; Backs et al. 2024; Bernini-Peron et al. 2024). However, JWST observations of galaxies at redshift  $z > 3$  reveal even lower metallicities up to  $\sim 2\% Z_{\odot}$  (e.g., Curti et al. 2024; Boyett et al. 2024). Therefore, it is essential to spectroscopically analyze stars in environments with sub-SMC metallicities to bridge the gap between theoretical predictions and high- $z$  observations. While old, low-mass, and extremely metal-poor ( $Z < 10\% Z_{\odot}$ ) stars can be found in the Milky Way and Galactic halo (e.g. Gratton & Sneden 1988; Cohen et al. 2008), young massive stars are missing there. A few massive stars with comparably low metallicities have been studied in comparatively distant ( $\gtrsim 1$  Mpc) compact dwarf galaxies such as Sextans A and Leo P (e.g., Evans et al. 2019; Garcia et al.

2019; Telford et al. 2024). The observations of individual massive stars in such distant locations suffer from limited signal-to-noise ratios and spatial resolution.

The Magellanic Bridge, first discovered by Hindman et al. (1963), is a stream of gas and mostly young stars connecting the two Magellanic Clouds. With its nearby distance of  $\sim 55$  kpc (Jacyszyn-Dobrzniecka et al. 2016), low foreground extinction, low density, and low mean metal content (Lehner et al. 2001), the Magellanic Bridge is a unique alternative laboratory in our cosmic neighborhood to study star formation and feedback at extremely low metallicity. Notably, Dufton et al. (2008) reported B stars in the Bridge with very low iron abundances.

The Magellanic Bridge contains a population of young stars (primarily B and A types) (Rolleston et al. 1999), but only recently the first three O-type stars were discovered (Ramachandran et al. 2021). Two of them were found to have extremely low mean CNO abundances of 4% and 8% solar. However, a main element affecting the mass loss and therefore evolution of massive stars is iron (e.g., Abbott 1982; Chiosi & Maeder 1986). The iron abundance and opacity set the necessary conditions to launch the wind of massive stars and thus are the main ingredient of the scaling of the mass-loss rate with metallicity (e.g., Pauldrach 1987; Vink et al. 2001). However, in contrast to most metals that are promptly expelled to the interstellar medium during the core collapse of massive stars, iron is mainly produced with a considerable time delay during supernovae type Ia. Thus, the iron abundance does not necessarily scale with other metal abundances. Differences between  $\alpha/\text{Fe}$  have also been discovered for some massive stars, e.g., in IC 1613 (Garcia et al. 2014). For hot OB stars, determining the iron abundance requires high-resolution UV spectra and is often unfeasible for distances larger than the Magellanic Clouds. Rapid rotation, common at low metallicity further complicates analysis by smearing iron lines. Thus, determined iron abundances are often limited to cool supergiants with iron lines present in optical spectra (Urbaneja et al. 2023).

In this work, we use newly acquired HST UV spectra to measure for the first time the inherent iron abundances for the two O-type stars MBO2 and MBO3 in the Magellanic Bridge (Ramachandran et al. 2021), which show low mean CNO abundances and slow rotation. For this, we employ atmosphere models with low iron abundances and a newly developed Bayesian analysis framework.

## 2. Observations

The UV spectra (ID. #16647, PI Ramachandran) of the two CNO metal poor O-type stars were taken with the grating G160M/1623 by the Cosmic Origins Spectrograph (COS) (Green et al. 2012) onboard the Hubble Space Telescope (HST).

To assess the consistency of our approach, we re-examined the iron abundance of one of the sample stars from Dufton et al. (2008) (DI 1388) which is reported to have the lowest iron content of only  $X_{\text{Fe}} = 1.26\% X_{\text{Fe},\odot}$ . Instead of the HST/GHRS/G200M spectra (1888 – 1929 Å) used by Dufton et al. (2008), our analysis is based on STIS/E140M spectra (ID. #7511, PI Keenan), which have a higher resolution and signal-to-noise ratio.

A summary of the stars' coordinates, spectral types (from Ramachandran et al. 2021), and observational settings can be found in Table A.1. In Figure 1, the location of the analyzed stars within the Magellanic Bridge is highlighted in respect to the SMC and LMC. The basic data reduction (e.g., normalization, radial velocity correction) is described in Appendix A.

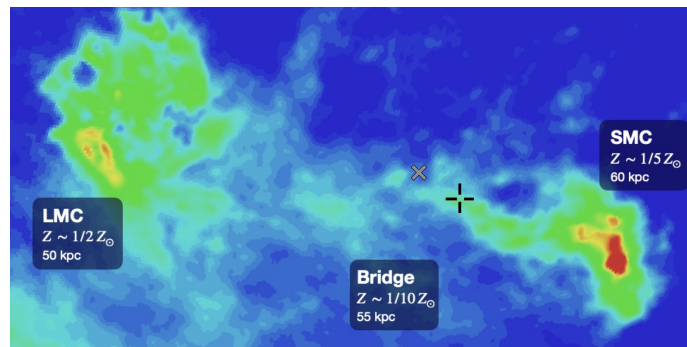


**Fig. 1.** Neutral hydrogen map of the Magellanic Clouds and the Magellanic Bridge from the HI4PI survey (HI4PI Collaboration et al. 2016). The black plus symbol marks the approximate position of MBO2 and MBO3 within the Magellanic Bridge, and the grey cross for DI1388.

## 3. Data Analysis

### 3.1. Stellar Atmosphere Models

For the spectral analysis, we use the PoWR non-LTE expanding stellar atmosphere code (see, e.g., Gräfener et al. 2002; Hamann & Gräfener 2003; Sander et al. 2015) which calculates model atmospheres and generates synthetic spectra for a chosen set of wind and stellar parameters. PoWR accounts for line blanketing by grouping thousands of atomic energy levels from iron group elements into superlevels (Gräfener et al. 2002). Adopting the parameters (such as  $T_{\text{eff}}$ ,  $\log g$ ,  $v \sin i$ ,  $v_{\text{mac}}$  etc.) and abundances from Ramachandran et al. (2021) constrained from the optical regime, we calculate models with different iron abundances between 1 and 15 % and varying microturbulent velocities (see Table D.1 for details on the used atomic data). Instead of the iron mass fraction directly, PoWR uses the iron group abundance (herein denoted as  $G$ ) as input parameter, consisting of scandium, titanium, vanadium, chromium, manganese, iron, cobalt, and nickel. The specific elemental abundances are calculated internally, weighted by their relative solar abundances. We do not analyze the wind features in this work, but instead employ fixed values for the terminal wind velocities of  $v_{\infty} = 1994 \text{ km s}^{-1}$ , and mass-loss rates of  $\dot{M} = 10^{-9.0} M_{\odot} \text{ yr}^{-1}$  and  $\dot{M} = 10^{-8.5} M_{\odot} \text{ yr}^{-1}$  for MBO2 and MBO3, respectively. Throughout this work, our reference for the solar abundances are the values from Asplund et al. (2009) and Scott et al. (2015a,b).

### 3.2. Determination of the microturbulence

Both stars, MBO2 and MBO3, have very narrow lines. For MBO2, Ramachandran et al. (2021) could only determine upper limits for the microturbulence  $\xi$ , projected rotation velocity  $v \sin i$  and the macro-turbulence  $v_{\text{mac}}$  due to the extremely narrow absorption lines. As there is a known degeneracy between Fe abundance and  $\xi$  (e.g., Bouret et al. 2015) when using the UV iron forest to determine Fe abundances, we carefully examined a range of microturbulent velocities between 1 and 20  $\text{km s}^{-1}$  that still reproduce the shape of the observed metal lines.

To find out which range of microturbulences agree with the observed spectrum, we compare the observed S v  $\lambda 1501.8$  line with models calculated varying  $\xi$  (see Fig. 2). We use the S v line as it is the strongest and most isolated metal line in the considered UV spectral range. Microturbulence influences the broadened wings of these metal lines. While for MBO2, all models with  $\xi \leq 5 \text{ km s}^{-1}$  match with the wings of the absorption lines, viable microturbulence values for MBO3 are in the range

of  $\xi = 5 - 10 \text{ km s}^{-1}$ . Ramachandran et al. (2021) determined a microturbulence of  $\xi \leq 2 \text{ km s}^{-1}$  for MBO2 and  $\xi = 8 \text{ km s}^{-1}$  for MBO3, thus agreeing with these results. To later combine the fitting results for different  $\xi$ , we also quantify the fit to the S v line by computing the  $\chi^2$  value (see Appendix B).

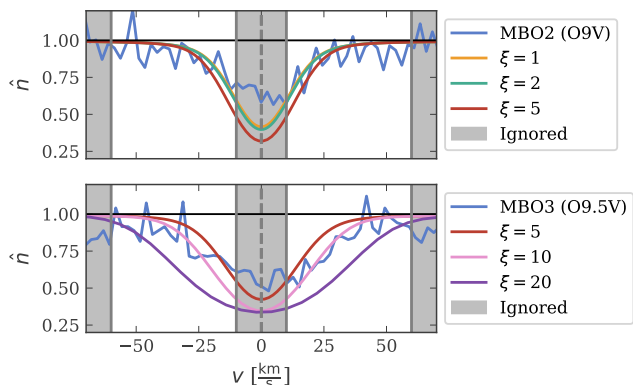


**Fig. 2.** Comparison of the observed and modeled S v  $\lambda 1501.76$  line for different  $\xi$  for MBO2 (top) and MBO3 (bottom) in velocity space. The defined wing region in which we evaluate  $\chi^2$  is highlighted.

### 3.3. Bayesian inference of iron abundances

Due to the difficulty of visually distinguishing Fe lines from the noise level, a more advanced approach than fitting by eye is required for accurate Fe abundance determination. As described in Appendix A, normalizing the UV spectra with synthetic models can require a small flux shift to the model continuum, corresponding to a slight change in stellar luminosity. Using Bayesian posterior sampling, we infer both the flux shift and the Fe group abundance  $G$  by fitting the forest of Fe IV-V lines for a range of fixed  $\xi$  values. To sample the posterior distribution, we employ the Markov Chain Monte Carlo (MCMC) algorithm emcee (Foreman-Mackey et al. 2013), assuming a Gaussian likelihood

$$\mathcal{L} = \prod_{i=1}^N \frac{1}{\sqrt{2\pi}\sigma_i} \exp\left(-\frac{(F_{\text{obs},i} - F_{\text{sim},i})^2}{2\sigma_i^2}\right). \quad (1)$$

and using the estimated flux errors  $\sigma_i$  from the COS data products (Johnson et al. 2021).

As the normalization varies across wavelengths, likely due to instrumental effects, and fitting the entire spectrum would require multiple shifts, we carefully restrict our fits to regions with reliable normalization. Additionally, we ignore the parts of the spectrum where the noise dominates, and spectral regions with wind lines or other strong absorption lines. These ignored wavelength intervals are different for both stars (see Appendix E) but are kept constant for all fits with different  $\xi$ .

We calculate a grid of PoWR models for each star with different iron metallicities, 8 models spaced between 1% and 15%  $G_{\odot}$  for MBO2 and 5 models between 1% and 9%  $G_{\odot}$  for MBO3, and otherwise fixed stellar parameters to the values determined from the optical spectrum in Ramachandran et al. (2021). To evaluate the spectrum at all metallicities within the grid, we use linear interpolation between the points. We use uninformative prior distributions: For the iron metallicity, we use a uniform prior in the interval given by the grid, and for the flux shift we use a truncated Gaussian prior centered around  $\mu_{\text{shift}} = 0$  and with standard deviation  $\sigma_{\text{shift}} = 10^{-14}$  in the interval  $[-3 \times 10^{-14}, 3 \times 10^{-14}] \text{ erg cm}^{-2} \text{ s}^{-1} \text{ \AA}^{-1}$ . For each star, we

run 10 chains with 10,000 steps. To confirm that the fits have converged, we check that the chain length is sufficiently ( $>50$  times) larger than the autocorrelation length  $\tau$ . We discard the first 1,000 burn-in steps and thin the samples so that we only consider each  $\tau/2$  step.

Finally, we compute the Fe abundance from the fraction of Fe in the G element (93%) and the total metallicity  $Z$  using the determined abundances for C, N, O, Mg, and Si from Ramachandran et al. (2021) plus our determined Fe abundance. The only missing element with a sufficient impact on  $Z$  is neon. As there is no Ne line detectable in the observed spectral range of the bridge stars, we estimate the Ne number fraction from the O number fraction using a scaling factor of 1/5.2 as was determined for the H II region NGC 346 within the SMC (Valerdi et al. 2019).

## 4. Results and Discussion

### 4.1. The metal-poor O stars MBO2 and MBO3

In Fig. 3, we compare the best-fit models with the observed Fe forest for MBO2 and MBO3. The microturbulence  $\xi$  is fixed to the values best reproducing the observed S v line (cf. Fig. 2), i.e.,  $2 \text{ km s}^{-1}$  and  $8 \text{ km s}^{-1}$  respectively. In addition, we show a posterior predictive sample, which is a set of simulated data points generated from the posterior distribution of model parameters. This sample allows us to assess the model's ability to reproduce the observed data. For both stars, the simulated and observed data agree well, indicating that the model successfully reproduces the key features of the observations within the uncertainties. The corresponding full spectra and corner plots for MBO2 and MBO3 can be found in Appendix E.

To study the degeneracy between  $\xi$  and Fe abundance, we also performed the fit for other  $\xi$ -values. The detailed individual fitting results including the corner plots and corresponding spectra can be found in Appendix E. A summary of the fitting results is depicted in Figure 4. As expected, the value for the iron abundance decreases when we assume a larger microturbulence. The derived iron abundances differ by a factor of two depending on which microturbulence is assumed, even though they all fit the metal line profile by eye similarly well as shown in Fig. 2.

By combining the posterior distributions for the different fixed  $\xi$  as described in Appendix B, we obtain a final iron mass fraction of  $1.41^{+0.10}_{-0.06} \times 10^{-4}$  ( $10.8^{+0.8}_{-0.5} \% X_{\text{Fe},\odot}$ ) for MBO2 and  $4.79^{+0.10}_{-0.32} \times 10^{-5}$  ( $3.66^{+0.07}_{-0.25} \% X_{\text{Fe},\odot}$ ) for MBO3. These values are lower than the adopted Fe abundance in the Ramachandran et al. (2021) models, but not different enough to affect the line predictions of other elements in the optical range. Given the unaffected main stellar parameters and C, N, O, Mg, and Si abundances, we can thus combine our results with the abundances from Ramachandran et al. (2021) and our Ne assumption (cf. Sect. 3.3) to obtain a metallicity of  $6.26 \times 10^{-4}$  ( $\sim 4.75\% Z_{\odot}$ ) for MBO2 and  $1.10 \times 10^{-3}$  ( $\sim 8.23\% Z_{\odot}$ ) for MBO3. The derived flux shift values are within  $5-7 \times 10^{-15} \text{ erg cm}^{-2} \text{ s}^{-1} \text{ \AA}^{-1}$  which corresponds to a shift of about 4-8% of the measured UV flux and is in the same range as the measured flux uncertainties.

A model-independent, direct comparison of the Fe lines between S3 in Sextans A (Telford et al. 2024) and MBO2 suggests a similar or lower Fe content for MBO2 (see Appendix C).

### 4.2. Comparison with the B star DI 1388

To check for systematic differences with the metal-poor B star study by Dufton et al. (2008), we analyzed DI 1388. We adopted the same stellar and broadening parameters from Hambly et al.

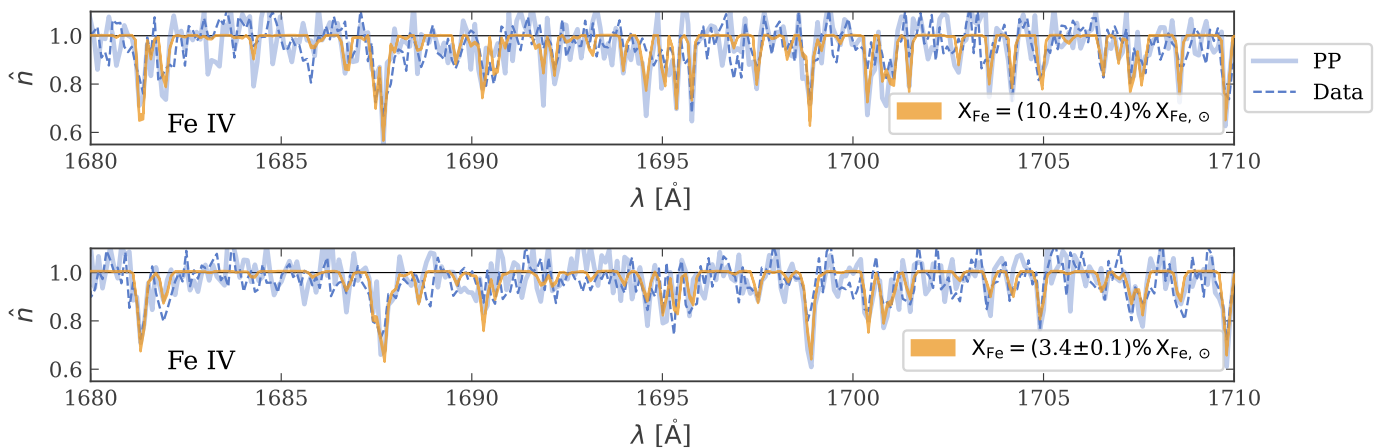


**Fig. 3.** Comparison of the observed (dashed, blue line) and best-fit modeled (orange) Fe iv forest of lines for fixed microturbulence values of  $\xi = 2 \text{ km s}^{-1}$  for MBO2 (top) and  $\xi = 10 \text{ km s}^{-1}$  for MBO3 (bottom). The thickness of the orange model line represents the  $3\sigma$  credible interval of the best-fit model. A posterior predictive sample (PP) is shown in light blue. Full spectral fits are given in Appendix E.

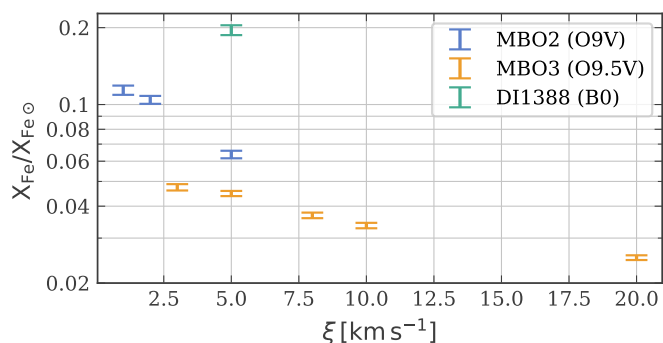


**Fig. 4.** Fit results for the iron abundances of MBO2, MBO3 and DI1388 as a function of different microturbulence values  $\xi$ .

(1994) as used by Dufton et al. (2008). We calculated a grid of models for DI 1388 with varying Fe abundances and a fixed microturbulence of  $\xi = 5 \text{ km s}^{-1}$ . Instead of the plane-parallel TLUSTY code (Hubeny 1988), we use the spherically-symmetric PoWR models and the same above-mentioned fitting procedure to derive the iron abundances.

In comparison to Dufton et al. (2008) ( $X_{\text{Fe}} = 1.26\% X_{\text{Fe}, \odot}$ ), we determine a much larger iron abundance of  $X_{\text{Fe}} = (21 \pm 1)\% X_{\text{Fe}, \odot}$  which is in the range of the mean SMC metallicity. The comparison of the best-fit model with the data is shown in Fig. E.18 and the corresponding corner plot in Fig. E.17. The difference in derived Fe abundance arises from a combination of factors, including differences in the i) underlined models ii) fitting methods, and iii) observational data. A major factor for the differences may be the different considered spectral wavelength ranges in Dufton et al. (2008) in comparison to this work. In contrast to Dufton et al. (2008), who used the range of 1890–1930 Å covering mainly the Fe III forest lines, we fit the models to the observed spectral range covering both the Fe IV and Fe V forest (see, e.g., Hillier 2020). At a temperature of  $\sim 32 \text{ kK}$ , Fe IV and Fe V are the dominant ions, which makes our chosen spectral range more suitable. Additionally, the HST/GHRS spectra have a much lower signal-to-noise ratio ( $S/N = 3$ ) in comparison to the STIS spectra ( $S/N = 10 - 25$ ) used in this work.

#### 4.3. Abundance patterns and signs for $\alpha$ enhancement

Our derived Fe abundances of O stars along with light metal abundances estimated from optical spectra (Ramachandran et al. 2021) suggest that they exhibit distinct chemical abundances despite their close spatial proximity (projected distance of  $\sim 15 \text{ pc}$ ). A summary of different metallicity measures of the analyzed stars can be found in Table 1. Both MBO2 and MBO3 are significantly metal-deficient, by more than a factor of two, compared to the average ISM metallicity reported by Lehner et al. (2008). In contrast, the more distant B star DI 1388 (projected distance  $\sim 3.3 \text{ kpc}$ ), exhibits SMC-like Fe and overall elemental abundances. An important result is that the iron abundances of MBO2 and MBO3 do not scale with the abundances of oxygen and other light elements. MBO2, although having the lowest mean abundance of light metals of  $\Delta [X/H] = -1.35$ , has a higher fraction of iron,  $[\text{Fe}/H] = -0.97$ . In contrast, MBO3 has a higher mean abundance of light metals of  $\Delta [X/H] = -0.98$  but a significantly lower iron content of  $[\text{Fe}/H] = -1.44$ .

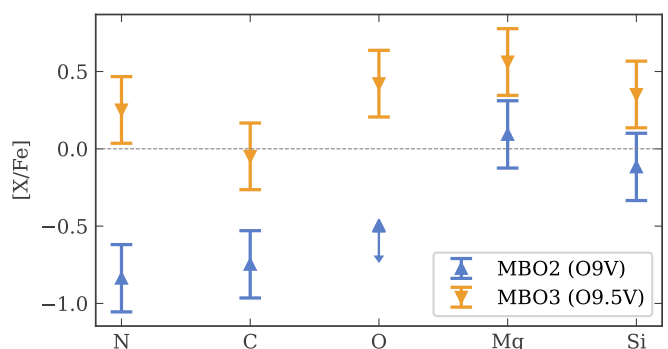


**Fig. 5.** Depletion of metals relative to iron. For MBO2, only an upper limit could be determined for the oxygen abundance (Ramachandran et al. 2021) which is highlighted by an arrow.

Figure 5 shows the  $X/\text{Fe}$  ratios (relative to solar values) for each element, including  $\alpha$  elements like O, Mg, and Si, illustrating how elemental abundances scale with iron. While  $\alpha$ -elements are mainly produced in massive stars and distributed to the ISM via their core-collapse supernovae, iron is primarily produced with a time delay through supernovae type Ia. MBO3,

**Table 1.** Comparison of abundance measurements of hot massive stars and the ISM in the Magellanic Bridge.  $[X/H]$  denotes the logarithm of the number fractions of X and H relative to their solar values.  $\Delta[X/H]$  denotes the mean over all light metals (N, C, O, Si, Mg). The metallicity Z is defined as the sum of all metal (N, C, O, Si, Mg, Ne, Fe) mass fractions. Spectral types of MBO2 and MBO3 are from Ramachandran et al. (2021).

Star	Sp. Type	$\left[\frac{\text{Fe}}{\text{H}}\right]$	$\left[\frac{\text{O}}{\text{H}}\right]$	$\Delta\left[\frac{X}{H}\right]$	Z	Source
MBO2	O9V	-0.97	-1.43	-1.35	$6.26 \times 10^{-4}$	This work
MBO3	O9.5V	-1.44	-0.98	-1.08	$1.10 \times 10^{-3}$	This work
DI 1388	B0	-1.9	-0.5	< -0.5		Dufton et al. (2008); Hambly et al. (1994)
		-0.68				This work
ISM		-0.61	-0.96			Lehner et al. (2008)

which has the lowest iron content, shows signs for significant  $\alpha$ -enhancement. In MBO2, O and Si are depleted relative to Fe, whereas Mg exhibits a slight enhancement.

Thus, the inhomogeneous ISM of the Magellanic Bridge, suggested by Ramachandran et al. (2021) based on light element abundances, is further confirmed by our analysis. We find a large scatter in Fe abundances ( $\sim 20 - 3\% Z_{\odot}$ ) and distinct  $[\alpha/\text{Fe}]$  ratios. These inhomogeneities may be linked to multiple gas accretion epochs, tidal interactions, or localized enrichment processes. To fully understand the complex chemical evolution of the Bridge, a more detailed and systematic chemical abundance analysis of a larger sample of young stars across the Bridge is essential (Schösser et al., in prep).

## 5. Conclusions

The low iron content of the stars and the inhomogeneities in their individual elemental abundances make the discovered O stars in the Magellanic Bridge unique counterparts to the high-redshift universe, where likely similar conditions existed. Our results suggest that inhomogeneous mixing occurs even at the present epoch. At earlier times, mixing would have been even less efficient. Thus, great caution is required when determining and interpreting abundances from integrated populations at high redshift. Already within the SMC and its outskirts, a variety of abundances is observed, most likely driven by interactions. At high redshift, these interactions were likely even more frequent, continuously changing the chemical content of the environment. Moreover, our results highlight that even for young stars, there is no simple scaling between oxygen and iron and the inference from one element to the other can lead to significant over- or underestimations. As iron is the main driver for winds and thus defines the main physics of the stars, these inaccuracies can lead to severe consequences for the inferred stellar evolution. This in turn leads to uncertainties in spectral energy distributions and ionizing radiation which affect chemical abundances derived from H II regions and contributions to cosmic reionization.

*Acknowledgements.* ECS acknowledges financial support by the Federal Ministry for Economic Affairs and Climate Action (BMWK) via the German Aerospace Center (Deutsches Zentrum für Luft- und Raumfahrt, DLR) grant 50 OR 2306 (PI: Ramachandran/Sander). ECS further acknowledges support by the Federal Ministry of Education and Research (BMBF) and the Baden-Württemberg Ministry of Science as part of the Excellence Strategy of the German Federal and State Governments. ECS, VR, AACS, MBP, and RRL acknowledge support by the German *Deutsche Forschungsgemeinschaft, DFG* in the form of an Emmy Noether Research Group – Project-ID 445674056 (SA4064/1-1, PI Sander). GGT acknowledges financial support by the Federal Ministry for Economic Affairs and Climate Action (BMWK) via the German Aerospace Center (Deutsches Zentrum für Luft- und Raumfahrt, DLR) grant 50 OR 2503 (PI: Sander). GGT and JJ further acknowledge funding from the Deutsche Forschungsgemeinschaft (DFG, German Research Foundation) Project-ID 496854903 (SA4064/2-1, PI Sander). ECS, MBP, JJ, and RRL are

members of the International Max Planck Research School for Astronomy and Cosmic Physics at the University of Heidelberg (IMPRS-HD).

## References

- Abbott, D. C. 1982, *ApJ*, 259, 282  
 Asplund, M., Grevesse, N., Sauval, A. J., & Scott, P. 2009, *ARA&A*, 47, 481  
 Backs, F., Brands, S. A., de Koter, A., et al. 2024, *A&A*, 692, A88  
 Bernini-Peron, M., Sander, A. A. C., Ramachandran, V., et al. 2024, *A&A*, 692, A89  
 Bouret, J. C., Lanz, T., Hillier, D. J., et al. 2003, *ApJ*, 595, 1182  
 Bouret, J. C., Lanz, T., Hillier, D. J., et al. 2015, *MNRAS*, 449, 1545  
 Boyett, K., Bunker, A. J., Curtis-Lake, E., et al. 2024, *MNRAS*, 535, 1796  
 Bromm, V., Coppi, P. S., & Larson, R. B. 2002, *ApJ*, 564, 23  
 Chiosi, C. & Maeder, A. 1986, *ARA&A*, 24, 329  
 Cohen, J. G., Christlieb, N., McWilliam, A., et al. 2008, *ApJ*, 672, 320  
 Curti, M., Maiolino, R., Curtis-Lake, E., et al. 2024, *A&A*, 684, A75  
 Dufton, P. L., Ryans, R. S. I., Thompson, H. M. A., & Street, R. A. 2008, *MNRAS*, 385, 2261  
 Evans, C. J., Castro, N., Gonzalez, O. A., et al. 2019, *A&A*, 622, A129  
 Foreman-Mackey, D., Hogg, D. W., Lang, D., & Goodman, J. 2013, *PASP*, 125, 306  
 Garcia, M., Herrero, A., Najarro, F., Camacho, I., & Lorenzo, M. 2019, *MNRAS*, 484, 422  
 Garcia, M., Herrero, A., Najarro, F., Lennon, D. J., & Alejandro Urbaneja, M. 2014, *ApJ*, 788, 64  
 Garg, P., Narayanan, D., Sanders, R. L., et al. 2024, *ApJ*, 972, 113  
 Gräfener, G., Koesterke, L., & Hamann, W. R. 2002, *A&A*, 387, 244  
 Gratton, R. G. & Sneden, C. 1988, *A&A*, 204, 193  
 Green, J. C., Froning, C. S., Osterman, S., et al. 2012, *ApJ*, 744, 60  
 Hamann, W. R. & Gräfener, G. 2003, *A&A*, 410, 993  
 Hambly, N. C., Dufton, P. L., Keenan, F. P., et al. 1994, *A&A*, 285, 716  
 HI4PI Collaboration, Ben Bekhti, N., Flöer, L., et al. 2016, *A&A*, 594, A116  
 Hillier, D. J. 2020, *Galaxies*, 8, 60  
 Hindman, J. V., Kerr, F. J., & McGee, R. X. 1963, *Australian Journal of Physics*, 16, 570  
 Hopkins, P. F., Wetzell, A., Wheeler, C., et al. 2023, *MNRAS*, 519, 3154  
 Hubeny, I. 1988, *Computer Physics Communications*, 52, 103  
 Jacyszyn-Dobrzyniecka, A. M., Skowron, D. M., Mróz, P., et al. 2016, *Acta Astron.*, 66, 149  
 Janka, H. T., Langanke, K., Marek, A., Martínez-Pinedo, G., & Müller, B. 2007, *Phys. Rep.*, 442, 38  
 Johnson, C. I., Plesha, R., Jedrzejewski, R., Frazer, E., & Dashtamirova, D. 2021, Updated Flux Error Calculations for CalCOS, Instrument Science Report COS 2021-03  
 Laseter, I. H., Maseda, M. V., Curti, M., et al. 2024, *A&A*, 681, A70  
 Lehner, N., Howk, J. C., Keenan, F. P., & Smoker, J. V. 2008, *ApJ*, 678, 219  
 Lehner, N., Sembach, K. R., Dufton, P. L., Rolleston, W. R. J., & Keenan, F. P. 2001, *ApJ*, 551, 781  
 Matthee, J., Mackenzie, R., Simcoe, R. A., et al. 2023, *ApJ*, 950, 67  
 Pauldrach, A. 1987, *A&A*, 183, 295  
 Ramachandran, V., Hamann, W. R., Oskinova, L. M., et al. 2019, *A&A*, 625, A104  
 Ramachandran, V., Oskinova, L. M., & Hamann, W. R. 2021, *A&A*, 646, A16  
 Rickard, M. J., Hainich, R., Hamann, W. R., et al. 2022, *A&A*, 666, A189  
 Rolleston, W. R. J., Dufton, P. L., McErlean, N. D., & Venn, K. A. 1999, *A&A*, 348, 728  
 Rowland, L. E., Stefanon, M., Bouwens, R., et al. 2025, arXiv e-prints, arXiv:2501.10559  
 Sander, A., Shenar, T., Hainich, R., et al. 2015, *A&A*, 577, A13  
 Scott, P., Asplund, M., Grevesse, N., Bergemann, M., & Sauval, A. J. 2015a, *A&A*, 573, A26  
 Scott, P., Grevesse, N., Asplund, M., et al. 2015b, *A&A*, 573, A25  
 Seaton, M. J. 1979, *MNRAS*, 187, 73  
 Telford, O. G., Chisholm, J., Sander, A. A. C., et al. 2024, *ApJ*, 974, 85  
 Urbaneja, M. A., Bresolin, F., & Kudritzki, R.-P. 2023, *ApJ*, 959, 52  
 Valerdi, M., Peimbert, A., Peimbert, M., & Sixtos, A. 2019, *ApJ*, 876, 98  
 Vink, J. S., de Koter, A., & Lamers, H. J. G. L. M. 2001, *A&A*, 369, 574  
 Vink, J. S., Mehner, A., Crowther, P. A., et al. 2023, *A&A*, 675, A154  
 Woosley, S. E., Heger, A., & Weaver, T. A. 2002, *Reviews of Modern Physics*, 74, 1015

## Appendix A: Data normalization and reduction

The UV spectra were obtained from Mikulski Archive for Space Telescopes (MAST) and are standard pipeline-processed data. We normalize the observed spectra (listed in Table A.1) by dividing them by a synthetic PoWR model continuum. As the shape of the spectral continuum does not change significantly for different iron metallicities between 1 and 15 %, we use a model with a fixed iron group mass fraction of 5%  $G_{\odot}$  to normalize the UV spectra. Additionally, we applied a small flux shift to the synthetic model continuum. These shifts remained consistent with measured photometry. For the Bayesian inference of the iron abundances (see Section 3.3), we treated this flux shift as a free parameter in our fitting process, as it is difficult to distinguish between the uncertainty level and the absorption lines. Thus, instead of normalizing the spectrum once, we repeat the process for all iterations during the Bayesian sampling process.

We then apply a radial velocity shift to the model spectra, 169 km s<sup>-1</sup> and 163 km s<sup>-1</sup> for MBO2 and MBO3 respectively. Furthermore, we account for galactic foreground and SMC reddening by applying the reddening law of Seaton (1979) with  $E_{B-V} = 0.08$  to all model spectra. Additionally, we convolve the model spectra with a Gaussian with FWHM = 0.1 to account for HST-COS's instrumental broadening, with a half-ellipse to account for rotation, and with a radial-tangential profile to account for macroturbulence.

## Appendix B: $\chi^2$ fit of the microturbulences

We quantify the goodness of the fit for different microturbulences by computing

$$\chi^2(\xi_i) = \sum_j \frac{(F_{\text{obs},i} - F_{\text{sim},i})^2}{\sigma_i^2}, \quad (\text{B.1})$$

which is the squared difference between the observed and model spectra, divided by the flux uncertainty  $\sigma_i^2$  at the  $i$ -th wavelength point. As we did not vary the sulfur abundance and we are only interested in the fit of the wings, we only compute  $\chi^2$  for the wing region of the S v line which we define by a velocity shift between 10 and 60 km s<sup>-1</sup> around the center of the line (see Fig. 2). The computed  $\chi^2$  values for models with different  $\xi$  for MBO2 and MBO3 are depicted in Fig. B.1.

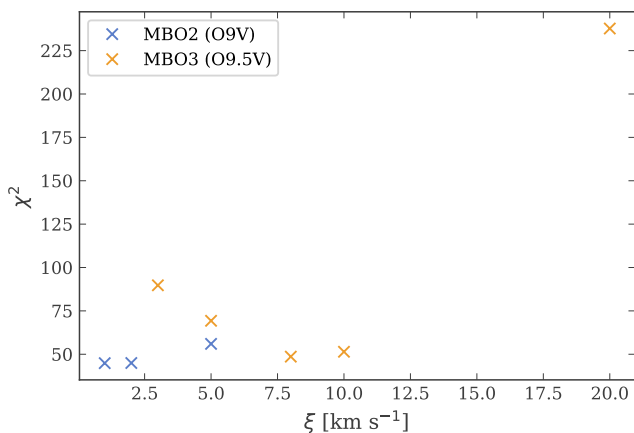


**Fig. B.1.** Computed  $\chi^2$  values for the wavelength range corresponding to the shaded region in Fig. 2 as a function of micro-turbulence for MBO2 and MBO3.

We derive the final iron abundances and associated uncertainties by considering the probability distribution of microturbulences. This is achieved by assigning normalized weights

$$w_i = \frac{\exp(-0.5 \chi^2(\xi_i))}{\sum_i \exp(-0.5 \chi^2(\xi_i))} \quad (\text{B.2})$$

to each microturbulence where we use the  $\chi^2$  value as derived from Equation (B.1). We combine the iron abundance posterior distributions as follows:

$$p(G) = \sum_i w_i p_i(G). \quad (\text{B.3})$$

## Appendix C: Comparison with S3

As a model-independent comparison of the metal content, we compare the UV spectrum of MBO2 with the star S3 in Sextans A in Fig. C.1, which have the same spectral type. To account for the significantly higher rotation of S3, we convolved the spectrum of MBO2 to match the observed  $v \sin i = 200$  km s<sup>-1</sup> of S3. Despite the noise in the spectrum of S3, MBO2's Fe lines appear similar to or weaker than those in S3, confirming the sub-SMC iron abundance of MBO2 and providing an independent consistency check of our new Fe abundance determination method.

## Appendix D: Atomic data

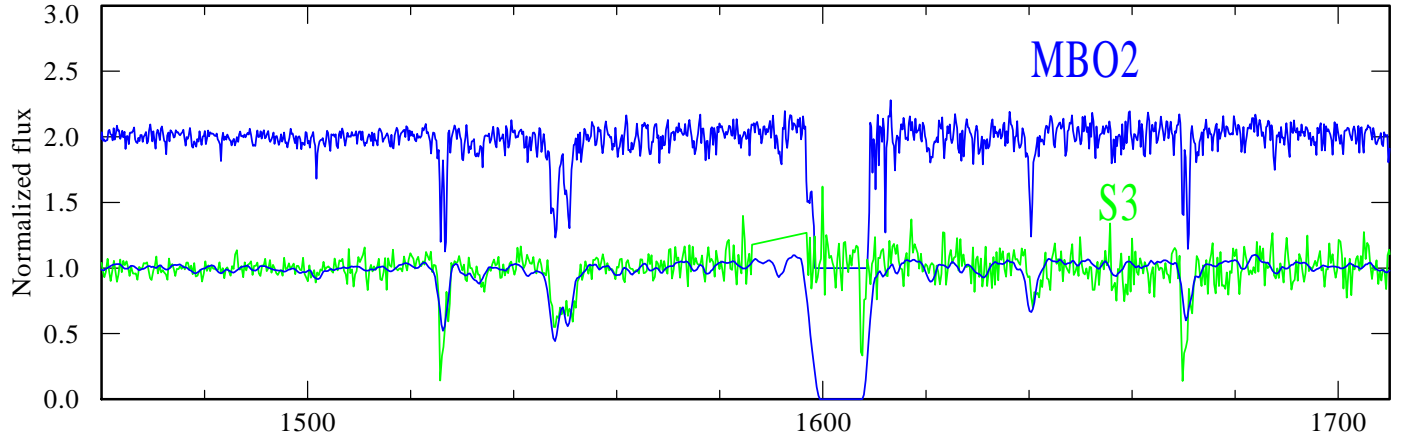
In Table D.1, we list the number of levels and line transitions accounted for in the detailed non-LTE atmosphere calculations with PoWR.

## Appendix E: Detailed fit results

In the following, we present the detailed fit results for MBO2, MBO3 and DI1388 including the corner plots and the best-fit model spectra over the full spectral range of HST/COS-G160M. The wavelength regimes that are ignored in the Bayesian analysis are highlighted by grey bands. For MBO2, we show the individual fit results for the microturbulences  $\xi = 1, 2$  and 5 km s<sup>-1</sup> (Figures E.1–E.6), for MBO3 for  $\xi = 3, 5, 8, 10$  and 20 km s<sup>-1</sup> (Figures E.7–E.16), and for DI1388 for  $\xi = 5$  km s<sup>-1</sup> (Figures E.17–E.18).

**Table A.1.** Details of the HST UV observations. The names and classifications of the stars are adopted from Ramachandran et al. (2021).

Star	RA [deg]	DEC [deg]	Spectral type	Grating	$\lambda$ [Å]	$R$	Exposure time [s]	S/N
MBO2	32.97933	-74.21028	O9V	COS/G160 M	1418 – 1789	19000	1220	15-35
MBO3	33.02008	-74.19933	O9.5V	COS/G160 M	1418 – 1789	19000	1200	15-35
DI1388	44.29958	-72.88194	B0	STIS/E140 M	1140 – 1735	45800	26160	10-25

**Fig. C.1.** Comparison of the UV spectrum of MBO2 (blue) convolved with a rotational broadening profile ( $v \sin i = 200 \text{ km/s}$ , matching S3) with the observed UV spectrum of S3 (green). The original, unbroadened MBO2 spectrum (shifted upward for clarity) is also displayed.

**Table D.1.** Overview of the number of levels and lines per ion handled in non-LTE in the calculated atmosphere models.

Elem.	ion	levels	lines	Elem.	ion	levels	lines
H	I	22	231	Ne	VII	1	0
H	II	1	0	Al	II	10	45
He	I	35	595	Al	III	10	45
He	II	26	325	Al	IV	10	45
He	III	1	0	Al	V	10	45
N	I	10	45	Mg	I	1	0
N	II	38	703	Mg	II	12	66
N	III	36	630	Mg	III	10	45
N	IV	38	703	Mg	IV	1	0
N	V	20	190	Si	II	1	0
N	VI	14	91	Si	III	24	276
C	I	15	105	Si	IV	23	253
C	II	32	496	Si	V	1	0
C	III	40	780	P	IV	12	66
C	IV	25	300	P	V	11	55
C	V	5	10	P	VI	1	0
C	VI	15	105	S	III	23	253
O	I	13	78	S	IV	11	55
O	II	37	666	S	V	10	45
O	III	33	528	S	VI	1	0
O	IV	25	300	G <sup>(S)</sup>	I	1	0
O	V	36	630	G <sup>(S)</sup>	II	3	2
O	VI	16	120	G <sup>(S)</sup>	III	13	40
O	VII	15	105	G <sup>(S)</sup>	IV	18	77
Ne	I	8	28	G <sup>(S)</sup>	V	22	107
Ne	II	1	0	G <sup>(S)</sup>	VI	29	194
Ne	III	18	153	G <sup>(S)</sup>	VII	19	87
Ne	IV	35	595	G <sup>(S)</sup>	VIII	14	49
Ne	V	54	1431	G <sup>(S)</sup>	IX	15	56
Ne	VI	49	1176	G <sup>(S)</sup>	X	1	0

**Notes.** <sup>(S)</sup> Meta element containing the iron group elements Sc, Ti, V, Cr, Mn, Fe, Co, and Ni. The level and line numbers denote superlevels and superlines for this element, which are treated in non-LTE. Each superlevel contains a large set of explicit levels (of the same parity) within an energy band. Superlines describe the combined treatment of all transitions between two superlevels and contain a complex, pre-calculated cross section incorporating all explicit line transitions between the levels within the two superlevels (see Gräfener et al. 2002, for more details).

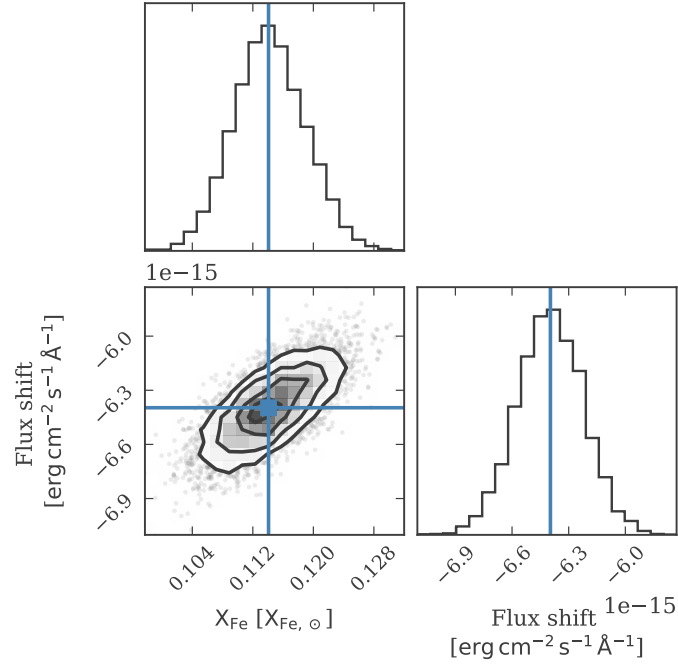


**Fig. E.1.** Corner plot for the fit of the iron mass fraction  $X_{\text{Fe}}$  and a flux shift in the spectral energy distribution for MBO2 and fixed microturbulence of  $\xi = 1 \text{ km s}^{-1}$ .

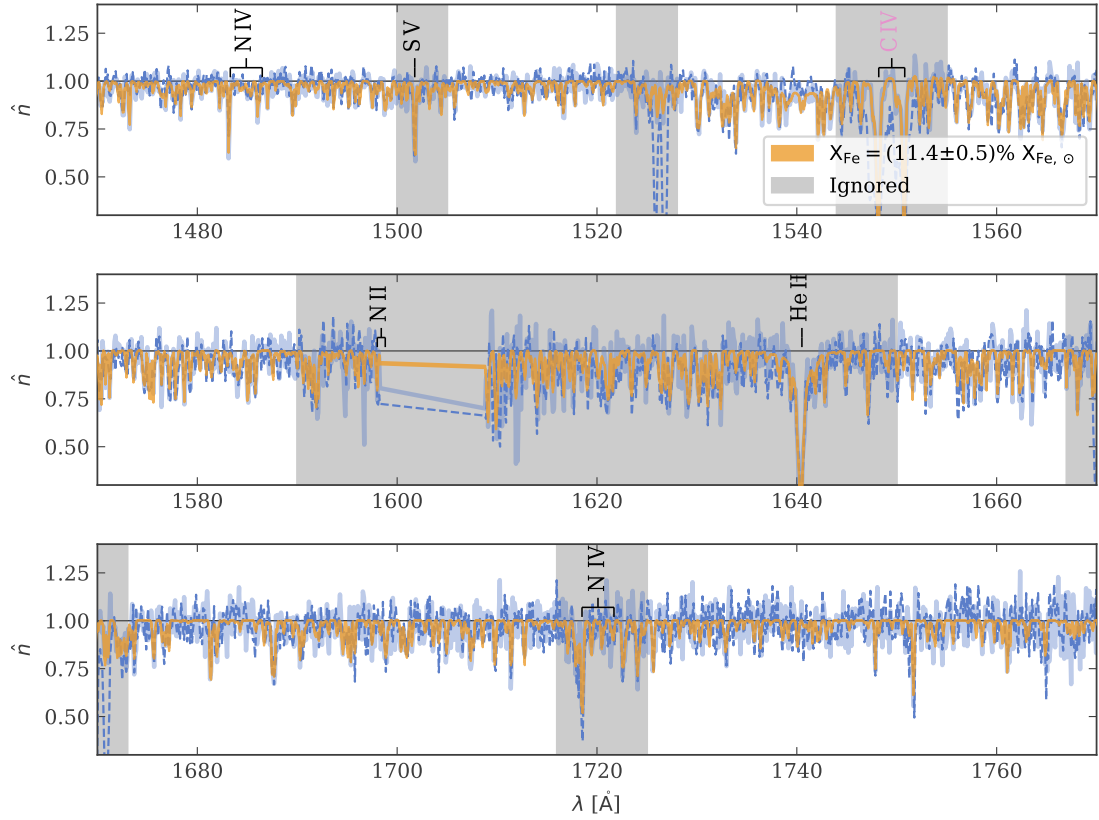


**Fig. E.2.** Comparison of the observed (dashed, blue line) and best-fit modelled spectrum (orange) for MBO2 and fixed microturbulence of  $\xi = 1 \text{ km s}^{-1}$ . The thick light blue line depicts a posterior predictive sample. Regions which are ignored in the fit are highlighted in grey.

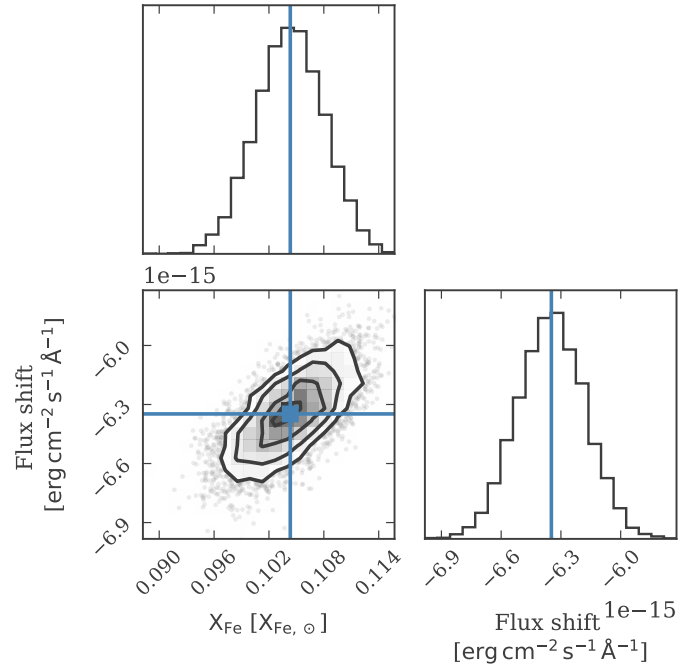


**Fig. E.3.** Corner plot for the fit of the iron mass fraction  $X_{\text{Fe}}$  and a flux shift in the spectral energy distribution for MBO2 and fixed microturbulence of  $\xi = 2 \text{ km s}^{-1}$ .

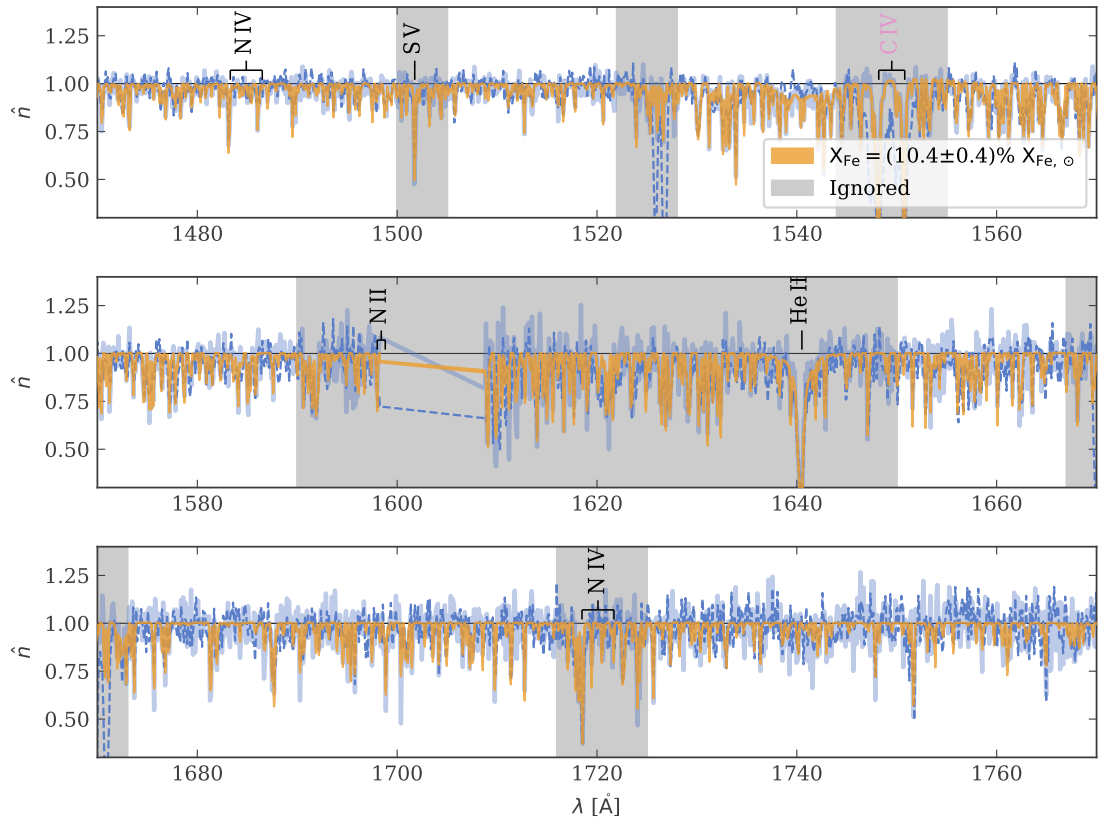


**Fig. E.4.** Comparison of the observed (dashed, blue line) and best-fit modelled spectrum (orange) for MBO2 and fixed microturbulence of  $\xi = 2 \text{ km s}^{-1}$ . The thick light blue line depicts a posterior predictive sample. Regions which are ignored in the fit are highlighted in grey.

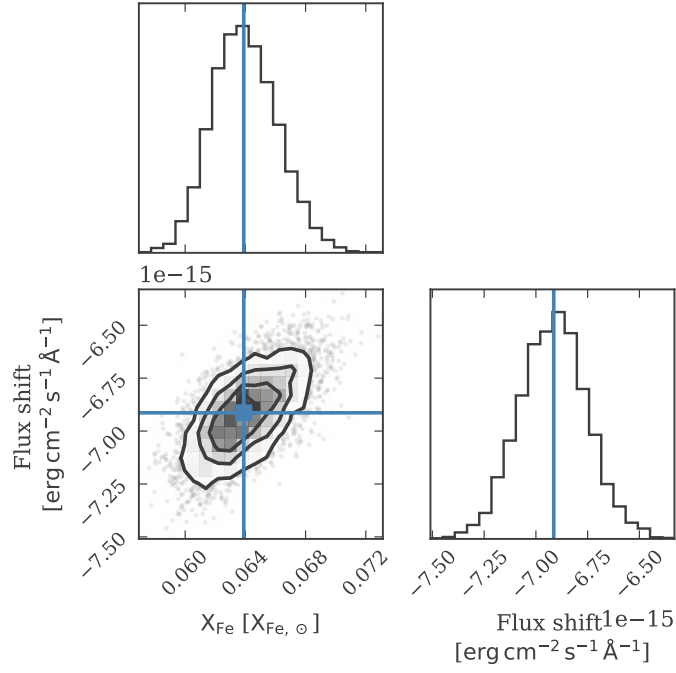


**Fig. E.5.** Corner plot for the fit of the iron mass fraction  $X_{\text{Fe}}$  and a flux shift in the spectral energy distribution for MBO2 and fixed microturbulence of  $\xi = 5 \text{ km s}^{-1}$ .

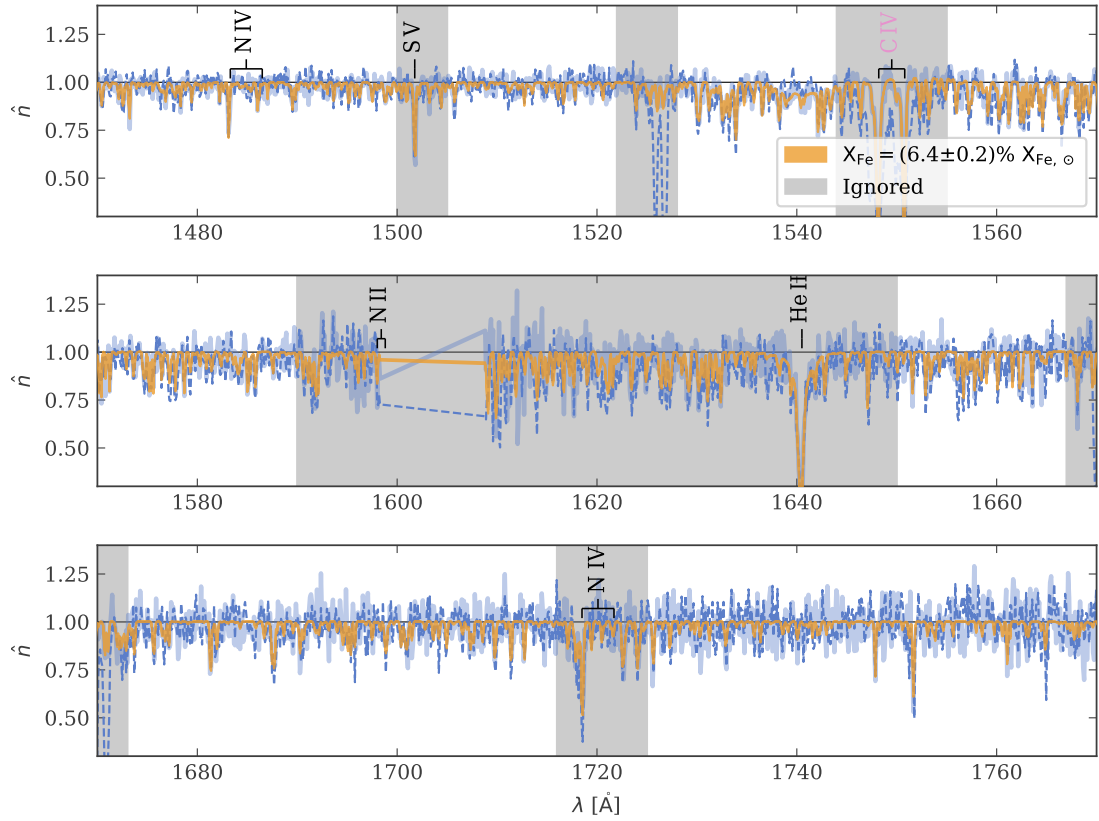


**Fig. E.6.** Comparison of the observed (dashed, blue line) and best-fit modelled spectrum (orange) for MBO2 and fixed microturbulence of  $\xi = 5 \text{ km s}^{-1}$ . The thick light blue line depicts a posterior predictive sample. Regions which are ignored in the fit are highlighted in grey.

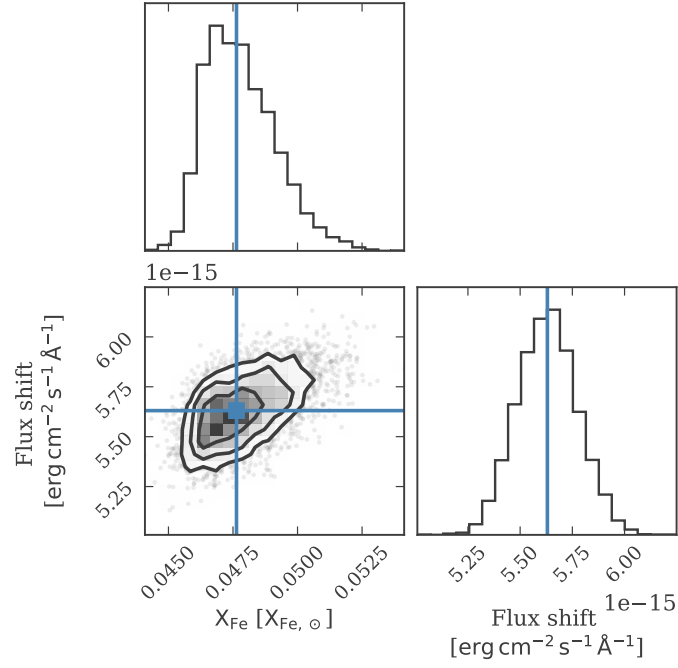


**Fig. E.7.** Corner plot for the fit of the iron mass fraction  $X_{\text{Fe}}$  and a flux shift in the spectral energy distribution for MBO3 and fixed microturbulence of  $\xi = 3 \text{ km s}^{-1}$ .

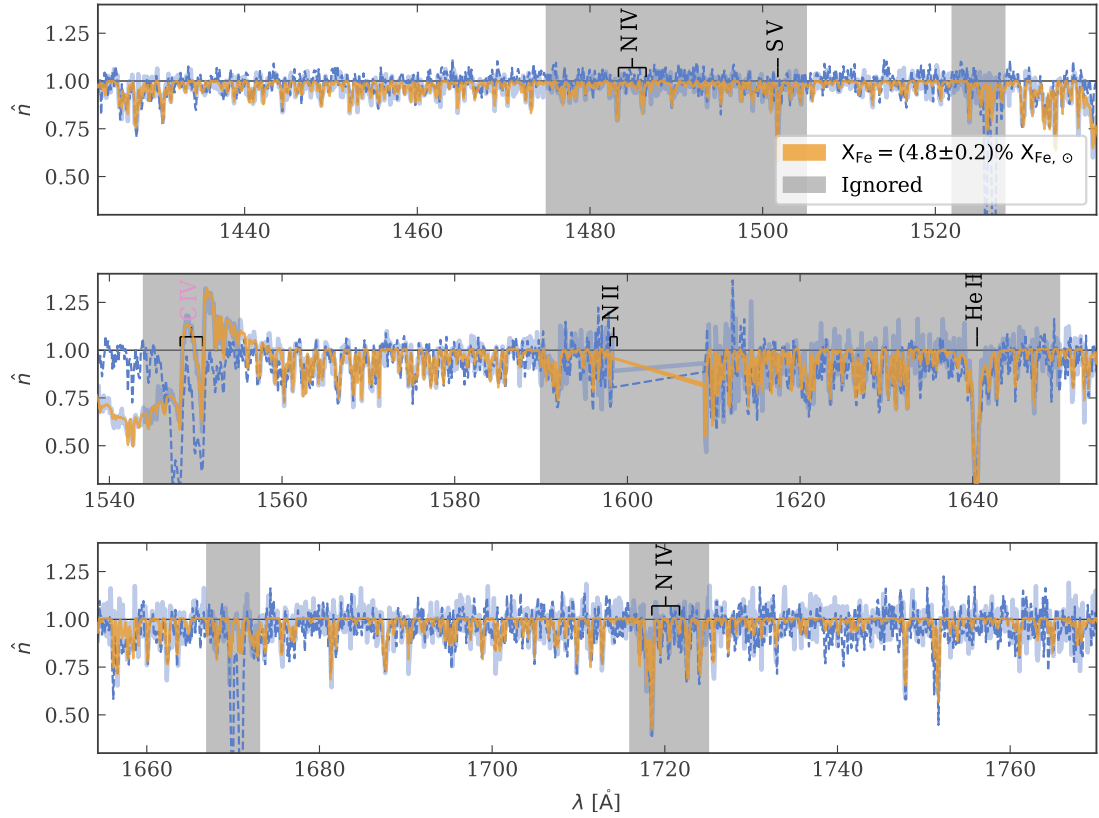


**Fig. E.8.** Comparison of the observed (dashed, blue line) and best-fit modelled spectrum (orange) for MBO3 and fixed microturbulence of  $\xi = 3 \text{ km s}^{-1}$ . The thick light blue line depicts a posterior predictive sample. Regions which are ignored in the fit are highlighted in grey.

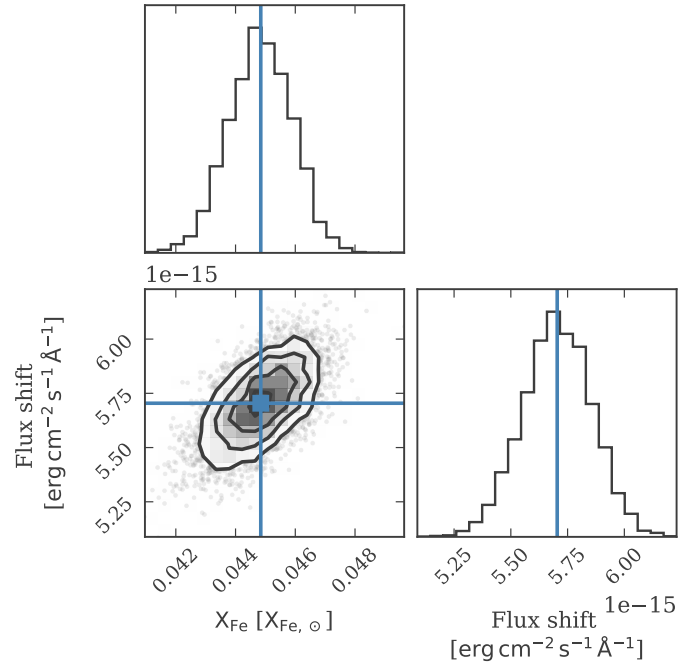


**Fig. E.9.** Corner plot for the fit of the iron mass fraction  $X_{\text{Fe}}$  and a flux shift in the spectral energy distribution for MBO3 and fixed microturbulence of  $\xi = 5 \text{ km s}^{-1}$ .

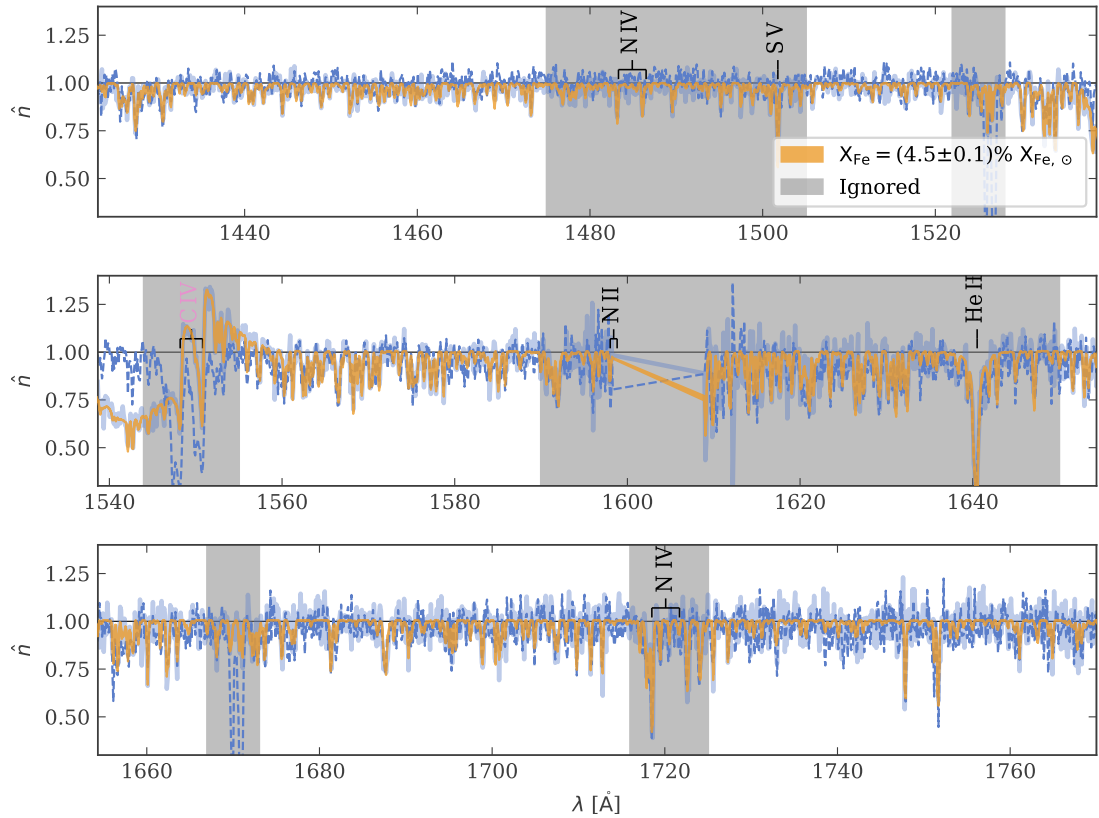


**Fig. E.10.** Comparison of the observed (dashed, blue line) and best-fit modelled spectrum (orange) for MBO3 and fixed microturbulence of  $\xi = 5 \text{ km s}^{-1}$ . The thick light blue line depicts a posterior predictive sample. Regions which are ignored in the fit are highlighted in grey.

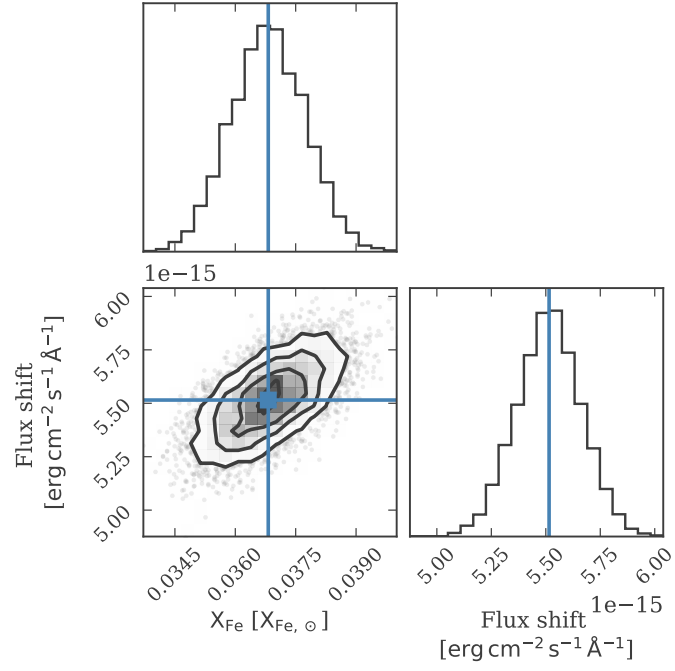


**Fig. E.11.** Corner plot for the fit of the iron mass fraction  $X_{\text{Fe}}$  and a flux shift in the spectral energy distribution for MBO3 and fixed microturbulence of  $\xi = 8 \text{ km s}^{-1}$ .

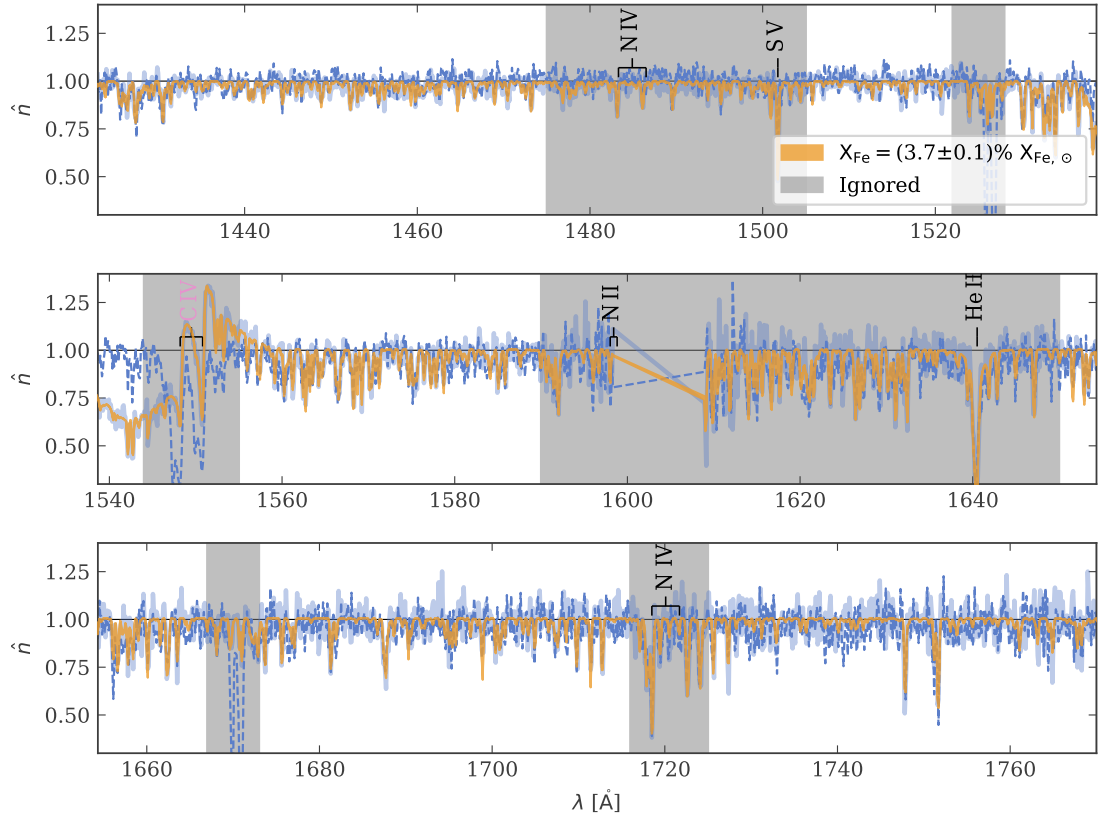


**Fig. E.12.** Comparison of the observed (dashed, blue line) and best-fit modelled spectrum (orange) for MBO3 and fixed microturbulence of  $\xi = 8 \text{ km s}^{-1}$ . The thick light blue line depicts a posterior predictive sample. Regions which are ignored in the fit are highlighted in grey.

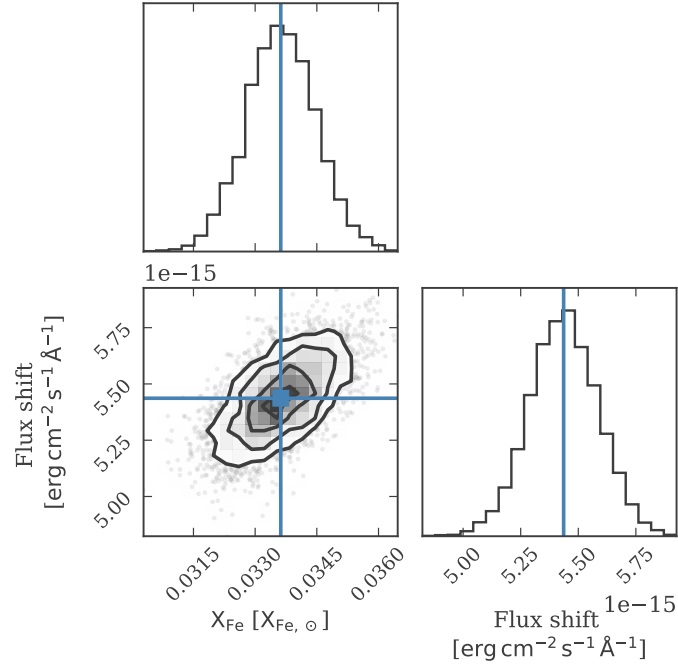


**Fig. E.13.** Corner plot for the fit of the iron mass fraction  $X_{\text{Fe}}$  and a flux shift in the spectral energy distribution for MBO3 and fixed microturbulence of  $\xi = 10 \text{ km s}^{-1}$ .

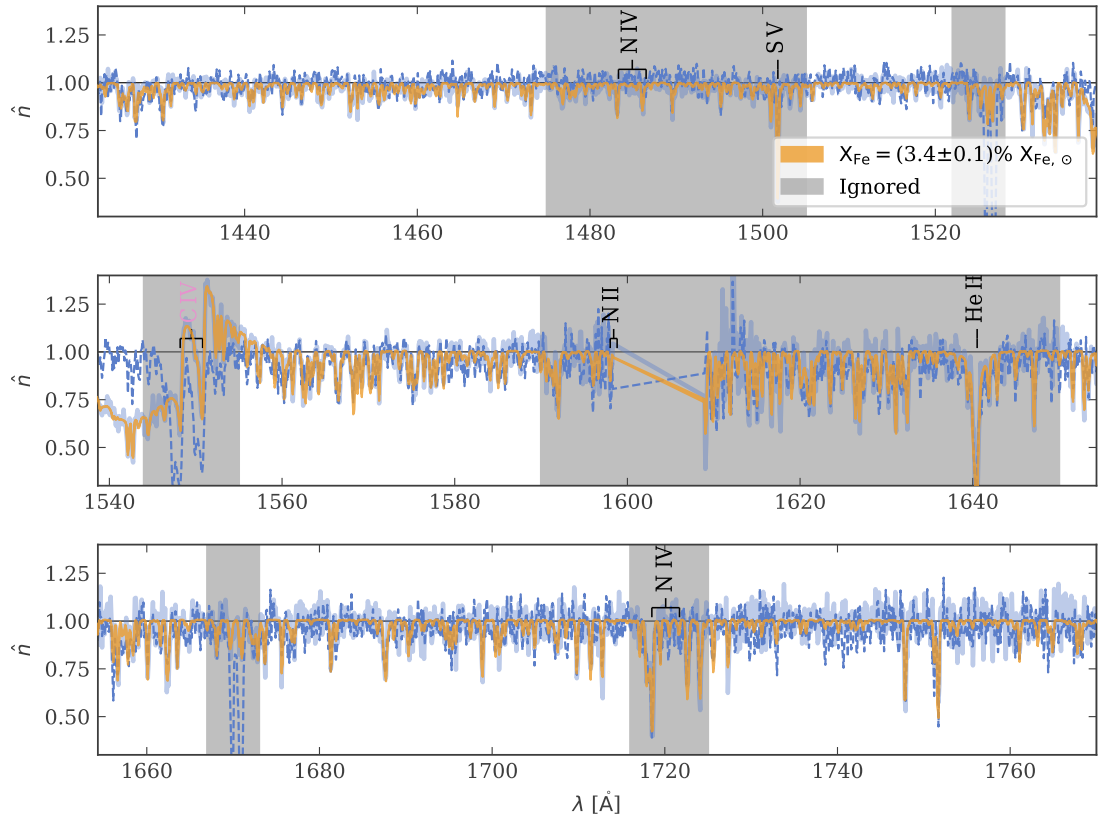


**Fig. E.14.** Comparison of the observed (dashed, blue line) and best-fit modelled spectrum (orange) for MBO3 and fixed microturbulence of  $\xi = 10 \text{ km s}^{-1}$ . The thick light blue line depicts a posterior predictive sample. Regions which are ignored in the fit are highlighted in grey.

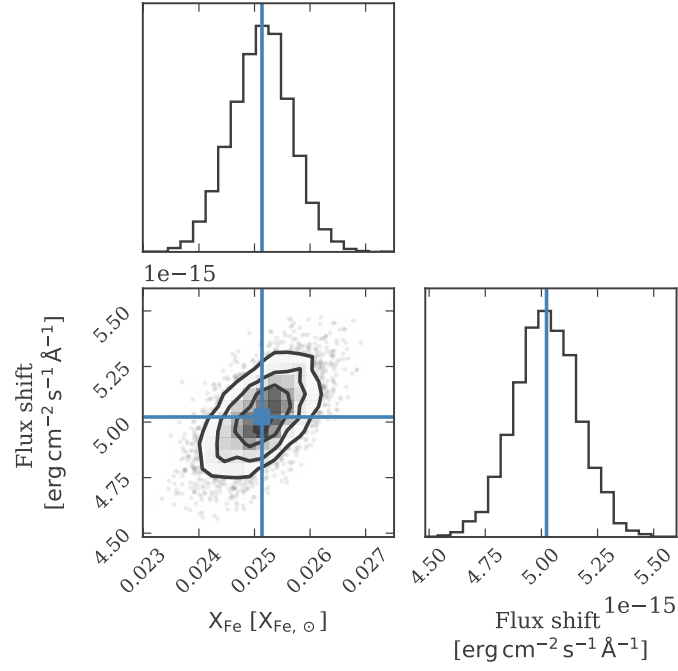


**Fig. E.15.** Corner plot for the fit of the iron mass fraction  $X_{\text{Fe}}$  and a flux shift in the spectral energy distribution for MBO3 and fixed microturbulence of  $\xi = 20 \text{ km s}^{-1}$ .

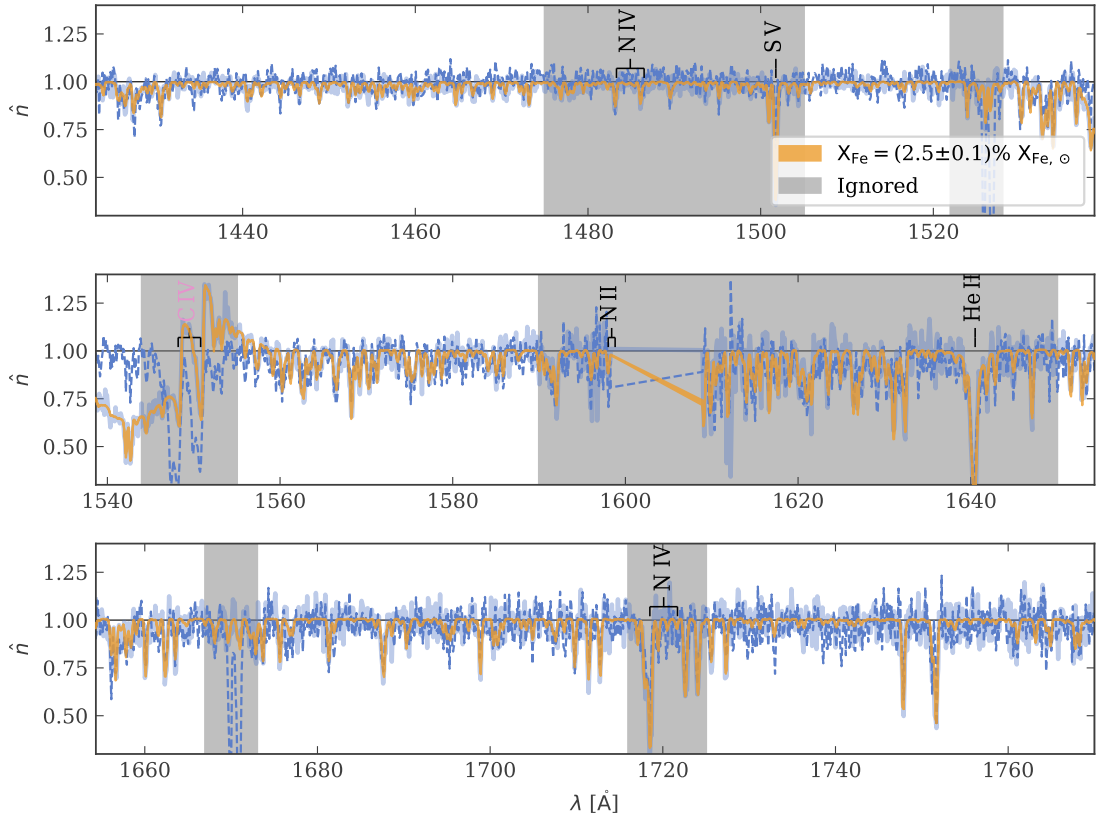


**Fig. E.16.** Comparison of the observed (dashed, blue line) and best-fit modelled spectrum (orange) for MBO3 and fixed microturbulence of  $\xi = 20 \text{ km s}^{-1}$ . The thick light blue line depicts a posterior predictive sample. Regions which are ignored in the fit are highlighted in grey.

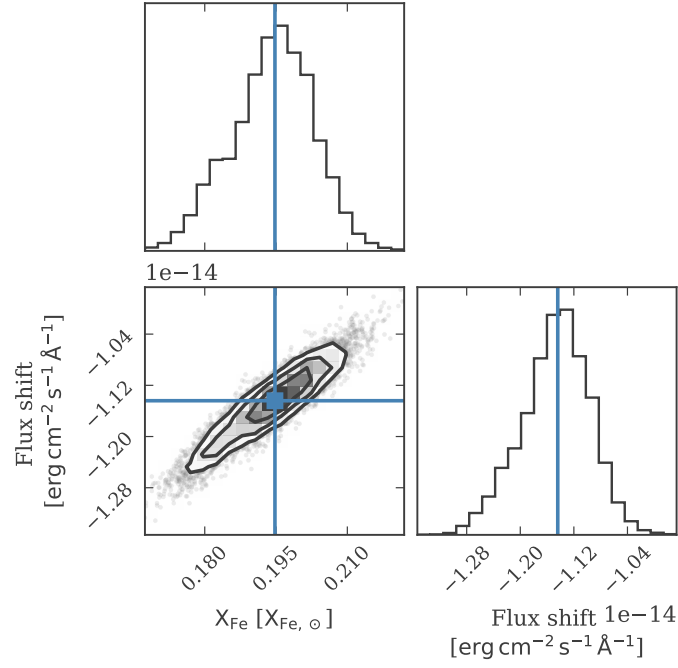


**Fig. E.17.** Corner plot for the fit of the iron mass fraction  $X_{\text{Fe}}$  and a flux shift in the spectral energy distribution for DI1388 and fixed microturbulence of  $\xi = 5 \text{ km s}^{-1}$ .

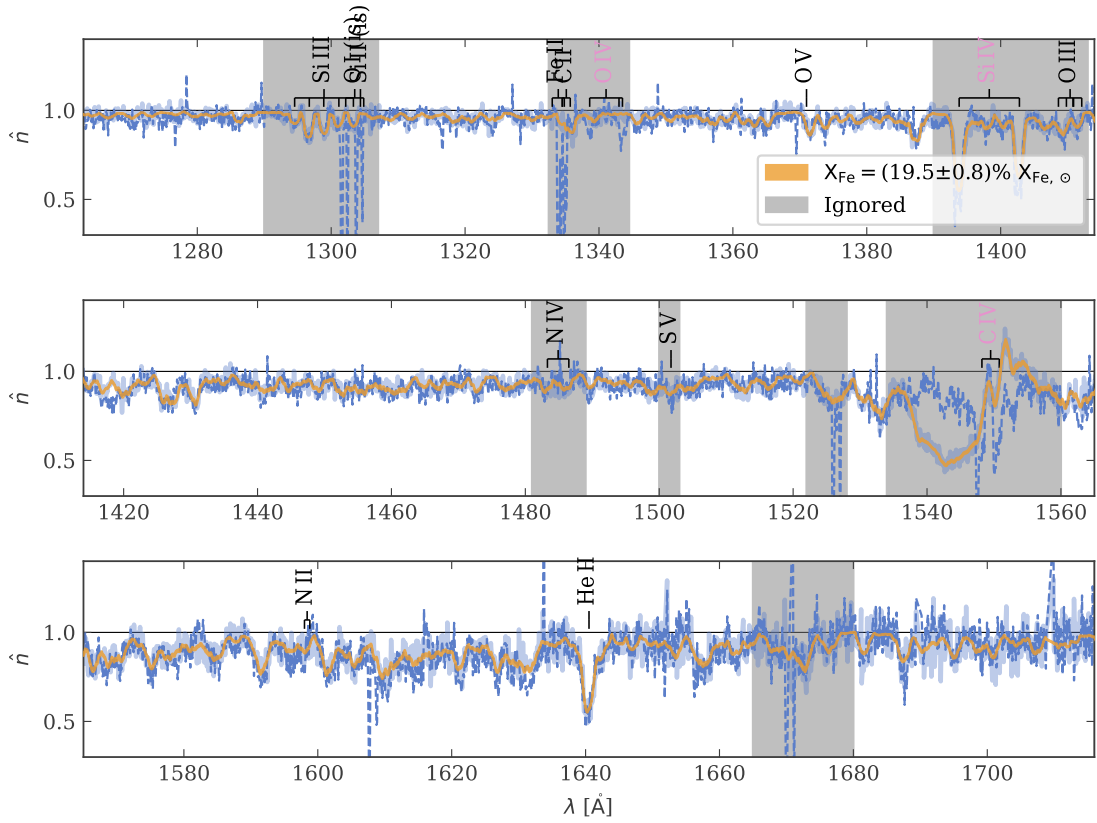


**Fig. E.18.** Comparison of the observed (dashed, blue line) and best-fit modelled spectrum (orange) for DI1388 and a fixed microturbulence of  $\xi = 5 \text{ km s}^{-1}$ . The thick light blue line depicts a posterior predictive sample. Regions which are ignored in the fit are highlighted in grey.